Rock Mech Rock Eng
DOI 10.1007/s00603-014-0591-z

ORIGINAL PAPER

Combined Scaling of Fluid Flow and Seismic Stiffness in Single Fractures

C. L. Petrovitch · L. J. Pyrak-Nolte · D. D. Nolte

Received: 4 April 2014 / Accepted: 10 April 2014

Abstract The connection between fluid flow and seismic stiffness in single fractures is governed by the geometry of the fracture through the size and spatial distributions of the void and contact areas. Flow and stiffness each exhibit scaling behavior as the scale of observation shifts from local to global sample sizes. The purpose of this study was to explore the joint scaling of both properties using numerical models. Finite-size scaling methods are used to extract critical thresholds and power laws for fluid flow through weakly correlated fractures under increasing load. An important element in the numerical fracture deformation is the use of extended boundary conditions that simulate differences between laboratory cores relative to in situ field studies. The simulated field conditions enable joint scaling of flow and stiffness to emerge with the potential to extrapolate from small laboratory samples to behavior on the field scale.

Keywords Hydromechanical scaling · Scaling · Fracture deformation · Rock fractures · Fracture

C. L. Petrovitch (✉)
Applied Research Associates Inc., Raleigh, NC, USA
e-mail: cpetrovitch@gmail.com

L. J. Pyrak-Nolte · D. D. Nolte
Department of Physics, Purdue University, West Lafayette, USA

L. J. Pyrak-Nolte
School of Civil Engineering, Purdue University, West Lafayette, USA

L. J. Pyrak-Nolte
Department of Earth, Atmospheric and Planetary Sciences, Purdue University, West Lafayette, USA

1 Introduction

The mechanical and hydraulic properties of a fracture depend on the morphology of rough surfaces. For example, fluid flow through a fracture depends on the size and spatial distribution of the apertures that are formed by placing two rough surfaces in contact (Brown 1989; Brown et al. 1995; Engelder and Scholz 1981; Lomize 1951; Neuzil and Tracy 1981; Pyrak-Nolte et al. 1987, 1988; Renshaw 1995; Tsang 1984; Tsang and Tsang 1987; Watanabe et al. 2008; Witherspoon et al. 1980). On the other hand, other studies have shown that fracture displacement depends on the surface roughness and the spatial distribution of contact area within a fracture (Bandis et al. 1983; Barton et al. 1985; Brown and Scholz 1985; Hopkins 1990; Hopkins et al. 1990; Kendall and Tabor 1971; Swan 1983; Yoshioka and Scholz 1989). Thus, it is plausible that through the properties of rough surfaces, their contact and their deformation, that a relationship between fluid flow through a fracture and fracture stiffness could exist (Cook 1992; Pyrak-Nolte 1996; Pyrak-Nolte and Morris 2000). However, prior to Petrovitch et al. (2013), no simple relationship had been determined because the mechanical and hydraulic properties depend on fracture geometry in different ways. Flow through a fracture is dominated by the dependence on the aperture distributions (both in size and in spatially), while fracture closure and fracture-specific stiffness depend primarily on the contact areas (Hopkins et al. 1990; Jaeger et al. 2007). These factors indicate that, while a fracture is under a normal load, flow requires geometric quantities beyond mean aperture to describe the system fully.

Witherspoon et al. (1980) conducted an experimental study to validate the cubic law for fractures under normal load. The cubic law is the solution to the Navier–Stokes

Published online: 03 May 2014

equation for flow between horizontal parallel plates with dimensions w and L, and separated by a distance h (the aperture). The cubic law is written as follows:

$$q = -\frac{wh^3}{12\mu}\frac{\partial P}{\partial x} \quad (1)$$

where w is the width of the channel, μ is the fluid viscosity, and $\partial p/\partial x$ is the pressure gradient over the length of the fracture, L. In Eq. (1), flow depends on the cube of the aperture. Thus, as stress is applied to a fracture, and the mean aperture decreases, flow through a fracture decreases.

In their experiment, Witherspoon et al. made measurements of fluid flow as a function of normal load while loading and unloading a tensile fracture in marble. In their work, they determined that the cubic law holds for low stresses when the mean aperture is large and the relative roughness is small. At high stress, they observed deviations from the cubic law. Zimmerman et al. (1990) and Zimmerman and Bodvarsson (1996) attributed deviations from cubic law to the condition when the dominant surface roughness wavelength is approximately equal to the hydraulic aperture. While Renshaw (1995) noted that the deviation from cubic law behavior occurred when the standard deviation in aperture remained nearly constant as the normal stress increased. The roughness and mean aperture play a vital role in fluid flow through a fracture, and Walsh (1981) used the solution for the flow through a channel with a circular blockage of radius a. This allowed the effects of contact to be included in the hydraulic aperture rather than the surface roughness. Thus, the combination of the decreasing mean aperture, increasing relative roughness, and increasing contact area allows fluid flow to change differently than the cube of the mean aperture.

At high stresses, Pyrak-Nolte et al. (1987, 1988) found that the exponent deviated from cubic law and observed values as high as 8–10. In this study, metal casting of the void spaces of natural fractures in granite was made under normal loads as high as 85 MPa. Cook (1992) described the void geometries at large stresses; "the existence of large oceanic regions of open fracture, [are] connected by tortuous paths through archipelagic' regions filled with numerous small, closely spaced contact regions". Pyrak-Nolte et al. concluded that as the stress increased, the large oceanic regions continued to deform, decreasing the mean aperture, while the small tortuous paths (that connect each larger region) controlled the flow. Since the small tortuous paths have relatively large aspect ratios (aperture height to channel width), the local stiffness was extremely large. Therefore, at large stresses, the flow rate is approximately stress independent while the mean aperture is not.

From the metal casting experiments (Pyrak-Nolte et al. 1987), Pyrak-Nolte (1996) hypothesized that an understanding of both the underlying void and contact geometries is required to explain the deviation from the cubic law. Pyrak-Nolte and Morris (2000) conducted numerical simulations to investigate the effect of the geometry of the fracture on the relationship between fluid flow and fractures stiffness. Using laboratory data from Witherspoon et al. (1980), Raven and Gale (1985), Gale (1982, 1987), and Pyrak-Nolte et al. (1987), the flow rates and stiffness were plotted parametrically. It was observed that within this data set, several of the flow rates for fractures did not vary considerably as a function of stiffness, while others decreased several orders of magnitude as the stiffness increased. From their computational efforts, Pyrak-Nolte and Morris (2000) attributed these differences to the spatial correlation length of the fracture void geometry. For their simulations, they used two types of fractures: those with short correlation lengths (random geometries) and those with long correlation lengths (large "oceanic" regions). After averaging fractures of each type, it was concluded that the flow–stiffness relationship is dependent on the correlation length of the void space geometry. Fractures with short-range correlation lengths maintained multiple flow paths that continued to support flow as the normal stress on the fracture increased. On the other hand, highly correlated fractures were composed of only one or two dominant flow paths that rapidly closed with increasing load and resulted in a rapid decrease in flow with increasing fracture-specific stiffness.

The work of Pyrak-Nolte and Morris (2000) demonstrated that fracture void geometry is the link between fluid flow and fracture-specific stiffness. In this paper, we present results of a numerical study that uses finite-size scaling to demonstrate the existence of a combined scaling relationship between fluid flow and fracture-specific stiffness.

2 Fracture Model

The relationship between fluid flow and fracture-specific stiffness is based on the assumption that these two fracture properties are implicitly linked through the fracture geometry (Pyrak-Nolte 1996; Pyrak-Nolte and Morris 2000). When two rough surfaces are brought together, regions of contact between the surfaces are formed as well as void with variable shape and aperture. Fracture geometry includes the probability and spatial distributions of both the contact area between the two fracture surfaces and the aperture distribution. Many methods have been used to generate fracture void geometry. Many numerical approaches simulate void geometries by generating two self-affine or self-similar rough surfaces that are then brought into contact to form the void geometry (Borodich and Onishchenko 1999; Glover et al. 1998; Peitgen and Saupe 1988; Walsh 1965). In this study, fracture geometry was generated by creating void spaces directly, rather than two rough surfaces, using a random 2D continuum percolation

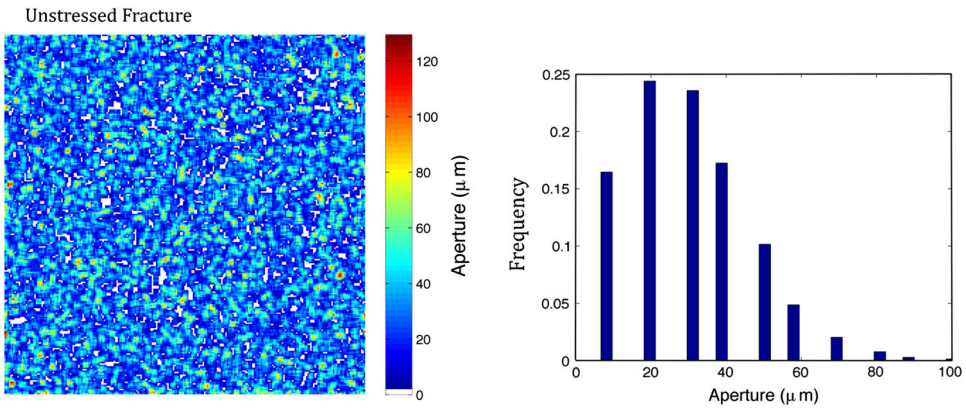

Fig. 1 Left: example of a spatially uncorrelated fracture void geometry. The *color* represents the size of the aperture. Right: histogram of the log-normal aperture distribution shown in the left (color figure online)

approach. The 2D continuum percolation approach provides synthetic fractures with log-normal aperture distributions and tunable correlation lengths. The percolation properties and fractal behavior of the synthetic fractures have been extensively studied (Nolte et al. 1989; Nolte and Pyrak-Nolte 1991, 1997; Pyrak-Nolte et al. 1992).

Fracture void geometry was created by randomly filling an initially zeroed 512 × 512 array by a selected number of points (NPTS). A point is defined by a point size which for this study was a 4 × 4 subarray (point size = 4). When a point is randomly plotted in the array, each array element is incremented by one. This increment in aperture as the points are plotted results in an aperture distribution. An example of the void geometry for a fracture with apertures with a short correlation length is shown in Fig. 1 (left). In this study, only weakly correlated fractures were generated. Each fracture has NPTS = 37,726 to achieve an initial void fraction of approximately 95 %. At the 512 × 512 scale, the fracture has an edge length of 1.0 m. A single point or pixel has an edge length of 1.95 mm. A point size = 4 results in a spatial correlation length of 7.8 mm (the grain size) and a log-normal aperture distribution (Fig. 1, right).

All fractures were generated on the 512 × 512 (1 m) scale and then subsectioned to study the scaling properties of fluid flow, fracture displacement, and fracture-specific stiffness. The subsections ranged from 256 × 256 down to 32 × 32, resulting in scales from 1, ½, ¼, 1/8, 1/16, and 1/32 of the original 512 × 512 pattern. Fluid flow and fracture deformation were calculated (using the numerical methods discussed in the following sections) for 100 fractures at each scale.

3 Deformation Model

3.1 The Hopkins Model

To determine the specific stiffness for a fracture, it is necessary to calculate fracture deformation by including the superposition of all far-field displacements in response to all the asperities as a function of stress. In this study, fractures were deformed numerically under a normal load using a method similar to that developed by Hopkins (1990). Hopkins approach assumes that a fracture can be approximated by two parallel half-spaces separated by an asperity distribution. This assumption is similar to Greenwood and Williamson's model (1966) where the joint was represented as an asperity distribution in contact with a flat and rigid surface, with later improvements by Brown and Scholz (1985) where a fracture was modeled as two rough surfaces in contact. Unlike these methods, Hopkins approach included the interaction between contact points by allowing each of the half-spaces to deform about the asperities in addition to and in response to the deformation of the asperity. No interpenetration of the two rough surfaces is allowed. This section provides a detailed description of the deformation model in the spirit of Hopkins (1990) and Pyrak-Nolte and Morris (2000).

In this approach, each asperity in the fracture is represented as a cylinder arranged on a regular lattice. Cylinders are used instead of the common Hertzian approach of two spheres in contact because the Hertzian solution is only valid when the radius of a contact is small compared with the radius of the sphere, it only gives compression of the tips of the asperities and it neglects the contribution to the deformation from the half-spaces. Hopkins (2000) showed that only 5 % of the total normal displacement at an isolated asperity is from compression of the asperity. The remainder of the displacement is from deformation of the half-spaces. In Hopkins (2000) approach, the increase in contact area with stress arises from the increase in the number of contacting asperities and contributes more to the increase in contact area than the deformation of the asperity tip in the Hertzian approach.

For each asperity, the height of a cylinder is determined by the fracture generation model (see Sect. 2) and is given a radius, a, such that all cylinders are initially in contact with their neighboring cylinders (Fig. 2, left). When a load

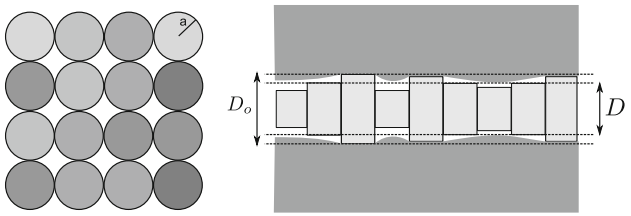

Fig. 2 Left: deformation model aligns the standing cylinders along a lattice-grid. The *shades of gray* represent different asperity heights. Right: an illustration of the half-spaces deforming around the asperities

is applied, the model deforms the half-spaces about the asperities (Fig. 2, right) and deforms the asperities due to the contact force of the half-spaces. The deformation of an asperity is given by

$$W_i = w_{ii} + \sum_{i \neq j} w_{ij} \tag{2}$$

where W_i is the total deformation at asperity i, and w_{ij} is the deformation at asperity i due to the deformation caused by asperity j. By allowing the half-spaces to deform, the total deformation at each asperity is a superposition of the self-interaction (displacement caused by the half-space, which is the first term in Eq. 2) and the asperity–asperity interaction (displacements caused by the deformation of the half-spaces via all other asperities, which is the second term in Eq. 2). The interaction displacement term is what differentiates Hopkins model from other approaches. For this study, the cylinders were given the physical properties of granite: Young's modulus, $E = 60$ GPa and Poisson's ratio, $n = 0.25$.

The deformation of the half-space was calculated using the Boussinesq solution for the normal deformation of a half-space under a uniformly loaded circle (Timoshenko and Goodier 1970). For points beneath the loaded circle ($r \leq a$), the deformation is given by

$$w_i(r \leq a) = \frac{4(1-v^2)qa}{\pi E} \int_0^{\frac{\pi}{2}} 1 - \frac{r^2}{a^2} \sin^2\theta \, \mathrm{d}\theta, \tag{3}$$

while the deformation for locations outside the circle ($r > a$) is given by

$$w_o(r > a) = \frac{4(1-v^2)qa}{\pi E} \times \left[\int_0^{\frac{\pi}{2}} 1 - \frac{a^2}{r^2} \sin^2\theta \, \mathrm{d}\theta - \left(1 - \frac{a^2}{r^2}\right) \int_0^{\frac{\pi}{2}} \frac{\mathrm{d}\theta}{1 - \frac{a^2}{r^2} \sin^2\theta} \right] \tag{4}$$

where q is the stress at each asperity and is equal to $f/(\pi a^2)$; f is the force on an asperity. The average displacement, d_{ij}, is determined by finding the total displacement at each asperity, i, caused by the force at j which is found by integrating Eqs. 3 and 4 over the entire area of the fracture, A, and dividing by the area of a single asperity:

$$\overline{d_{ij}} = \frac{1}{\pi a^2} \iint_A w_o(r, C) \mathrm{d}r\mathrm{d}\theta \tag{5}$$

where C is the set of asperities in contact. The total displacement, W_i, at asperity i caused by the deformation of all of the asperities is found by summing the average displacement caused by all of the asperities:

$$W_i = \sum_{j \in C} \overline{d_{ij}} \tag{6}$$

where C is the set of asperities in contact. The stress also results in the deformation of the asperity. The displacement of asperity i under a compressive load, f, is

$$\Delta h_i = \frac{f_i h_i}{\pi a^2 E} \tag{7}$$

where h_i is the initial height of asperity i, and f_i is the force at asperity i. The force exerted by a given asperity depends on the displacement of the half-spaces. In turn, the displacement of the half-spaces depends on the forces exerted by all of the other asperities. A system of linear equations is formed by recognizing that the initial sum of the distances between the half-spaces in the absences of asperities (D in Fig. 2) and the total deformation, W_i, must be equal to the length of the asperity

$$D + W_i = h_i - \Delta h_i \tag{8}$$

Equation 8 represents a system of simultaneous linear equations in terms of Δh_i because W_i depends indirectly on Δh_i through the force term in Eq. 7. The resulting system is large ($N^2 \times N^2$, where N is the number of asperities in contact), dense and computationally intensive to solve directly as it would require $O(N^4)$ operations. The conjugate gradient method was chosen to solve this system of linear equations because it reduces the problem to a matrix–vector multiplication. The computation time for the solver was reduced by recognizing that long-range interactions can be approximated accurately by performing a Taylor series expansion around the half-space's displacement for large radii. Using this approximation, the matrix–vector product can be rapidly calculated using the fast multipole method (FMM) (Pyrak-Nolte and Morris 2000). Additional details on the implementation of the FMM can be found in Petrovitch (2013).

The fracture-specific stiffness is calculated from the displacement–stress curve generated by the deformation models. The stiffness is defined as

$$\kappa(\sigma) = \frac{\mathrm{d}\sigma}{\mathrm{d}\delta} \tag{9}$$

where σ is the stress applied to the fracture and δ is the average displacement of the fracture given by

$$\delta_i = \begin{cases} D_o - D - W_i & \text{if not in contact} \\ D_o - h_i - \Delta h_i & \text{if in contact} \end{cases}$$
$$\delta = \sum_i \frac{\delta_i}{N} \qquad \text{for } N \text{ asperities in contact} \tag{10}$$

where D_o is the zero-stress spacing between the half-spaces (Fig. 2)

3.2 The Importance of Boundary Conditions

The approach described above computes the fracture deformation as a function of stress for the condition of free boundaries. This is similar to the conditions in the laboratory when a finite sample, like a core, is placed under a constant displacement load. Contact points near the edges have less support than those near the center, leading to a non-uniform closure. This is fundamentally different from what would be found in the field. Field measurements of fracture-specific stiffness using remote seismic methods would probe local parts of a larger fracture. For this reason, periodic boundary conditions (PBC) were used to simulate conditions similar to the field by introducing an "external" lattice of multipole moments in the FMM calculation (Lambert 1994).

Adding PBC to a system of interacting bodies (contact points in this case) requires detailed consideration. The system must be repeated infinitely in both the x and y directions. The system could simply be copied for a finite distance in each direction to approximate the infinite case, but, in using this method, the number of bodies grows too quickly to calculate. There are two common methods to overcome this: Ewald summations (Schmidt and Lee 1991) and the macroscopic expansion (ME) (Lambert 1994). In our work, the macroscopic expansion method was used because it reuses the FMM formalism already in place. The macroscopic expansion method begins by assuming the system is repeated according to a regular rectangular lattice, where each lattice point is a copy of the system of interacting bodies. Using the FMM formalism, the multipole moments of the system can be used at each lattice point, instead of directly copying the system.

For the macroscopic expansion method to work, three modifications were made to the standard FMM algorithm. First, the top level in the quad-tree must "feel" the effect of the lattice, thereby enabling the method to overcome the need to directly sum each lattice point. Second, the interaction lists of any given region must wrap periodically to the opposite side of the domain. Third, the direct sum of the interacting bodies at the highest resolution must wrap periodically to their near neighbors. Petrovitch (2013) gives a complete description of the equations and implementation of the macroscopic expansion method.

With the three modifications in place, the formalism of the ME method approximates PBC when deforming the fracture plane. Figures 3 and 4 provide a comparison of the effect of assuming PBC versus free boundary conditions. In Fig. 3, the aperture distribution of a fracture subjected to 10 MPa of normal stress is shown after normalizing by the initial unstressed aperture distribution. When a fracture is subjected to free boundary conditions, the fracture preferentially deforms around the perimeter of the fracture plane (Fig. 3a). The final perimeter apertures are a small fraction of the initial values, while the central apertures closed the least. The deformation is more uniform when PBC are used. Figure 4 is a histogram of the apertures taken from the top edge (or row) of the fractures shown in Fig. 3. The free boundary conditions cause greater deformation along the edge of the sample than the PBC. The histogram shows that the deformed fracture under free boundary conditions has significantly more small apertures along the edge. As will be shown in the next section, preferential closure of the apertures near the perimeter of the fracture strongly affects the percolation properties.

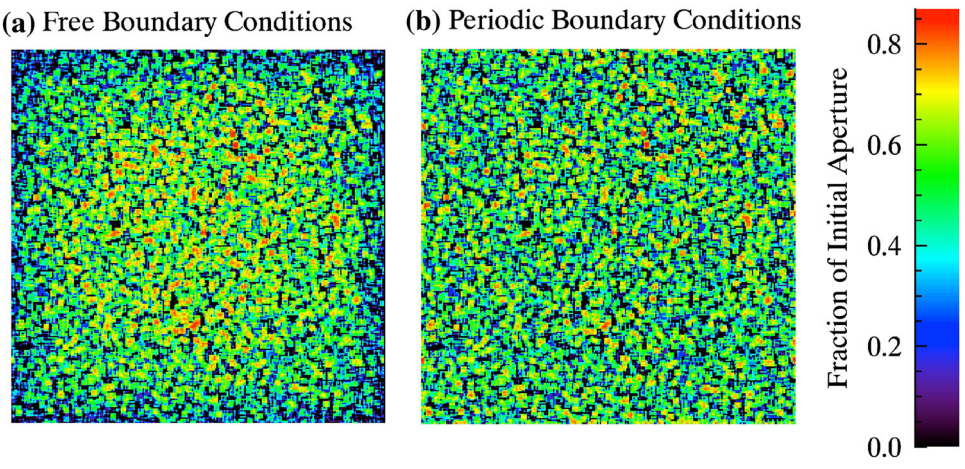

Fig. 3 Comparison of normalized aperture (*black*) distribution for **a** free boundary conditions and **b** PBC. The aperture distributions were normalized by the aperture distribution for the same fracture under no load

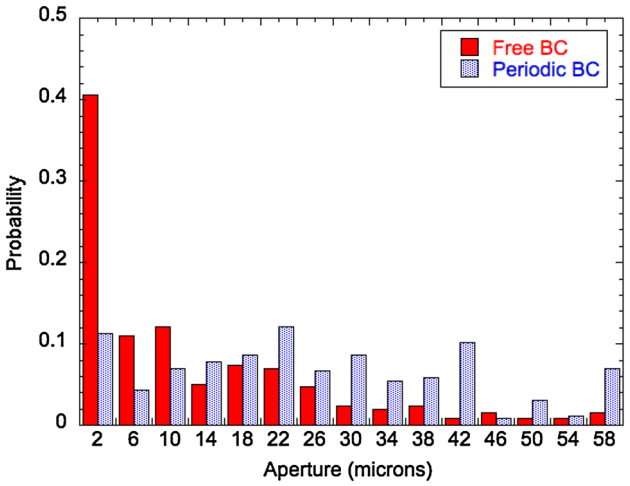

Fig. 4 Histogram of apertures along the top edge of the fractures shown in Fig. 3

4 Flow Model

A numerical model that calculates fluid flow through an aperture distribution is required to investigate the relationship between the mechanical and hydraulic properties of fractures. The hydraulic properties of the simulated fractures considered in this study were calculated numerically using a network model similar to that of Yang et al. (1989, 1995), Tran (1998), Cheng et al. (2004), and Pyrak-Nolte and Morris (2000). In this model, the aperture distribution is replaced by a connected graph where each edge on the graph represents an elliptical pipe. This model is not direction blind, i.e., global flow and local flow are assumed to be in a similar direction, namely the network is constructed from the inlet to the outlet. This elliptical pipe approach was experimentally validated by Cheng et al. (2004) and compared to numerical results when local flow is modeled by parallel plates, which is a simple lattice-grid method that is direction blind. Cheng et al. (2004) fabricated micro-models with either spatially uncorrelated or spatially correlated fracture geometry using photolithography, and the flow of water through the micromodels was measured experimentally. They found that the lattice-grid numerical method overpredicted experimentally measured flow by a factor of 1.5–2, while the elliptical pipe method agreed to within 10–30 % of the experimental values. This validates the assumption that the global and local flow directions are in a similar direction. In addition, the elliptical pipe method is computationally more efficient (run times are 4–10 times faster than the lattice-grid method).

To construct the pipe graph, each row of aperture elements perpendicular to the pressure gradient is considered in turn and large regions of nonzero apertures are brought together into a single large elliptical pipe. Rows will have regions where cross sections intersect. In these cases, the elliptical pipes are connected into a Y-shaped joint. Flow is calculated based on the analytic solution to flow in an elliptical pipe with a hydraulic resistance based on the apertures,

$$R = \frac{4f\mu\Delta l\sqrt{K}(K+1)}{\pi a}, \tag{11}$$

where

$$f = \frac{\pi(a_1 b_1 + a_2 b_2)}{2A_{\text{avg}}}, \tag{12}$$

$$K = {}^{a^2}/_{h^2}. \tag{13}$$

The parameters a_i and b_i for $i = 1, 2$ are the major and minor axes of the two ellipses between rows, a is the average minor axis between the rows, h is half the maximum aperture of the larger ellipse, Δl is the distance between the center of the two elements, and A_{avg} is the average area of the two ellipses. All of the nodes on the inflow and outflow edges are connected into a source and sink node, respectively, to provide a point to set the pressure boundary conditions. At this point, the graph contains nodes and edges that contain all of the void spaces of the fracture. The aperture map consists of void spaces that can be isolated from the main percolation cluster that spans from sink to source. The isolated clusters do not contribute to the flow in any way, and if left in the graph, they cause the matrix equation to become singular. A depth-first search is performed to remove the isolated clusters.

After the depth-first search, a graph that corresponds to the network of pipes is formed where each node in the graph is a vertex where pipes meet and each pipe is fit to shape the aperture map with an ellipse. A sparse linear system of equations is written based on the graph connections to compute the flow through the entire fracture (see Petrovitch (2013) for additional details). The *Dist Library* from Oak Ridge National Laboratory (Ng and Peyton 1993) was used to solve the system of equations by performing a Cholesky factorization on the node conductance matrix. From this method, the flow velocities and pressures are computed at each connected point in the void spaces of a fracture. The assumed fluid was water with a viscosity of 0.001 Pascal-seconds. It should is noted that PBC were not used for the flow model. In this study, the scaling associated with subsamples of a larger fracture was investigated and the pressure gradient per unit length was kept constant to simulate correctly this effect.

5 Finite-Size Scaling

We examine the scaling behavior of the mechanical behavior separately from the scaling of the hydraulic

properties of a fracture in the first section before addressing the joint scaling relationship between these two fracture properties.

5.1 Concept of Critical Scaling

The concept of critical scaling comes from the statistical mechanics of phase transitions like the percolation transition in fluid flow. When measuring the properties of a system in a critical regime, properties become scale dependent. In general, a physical property, χ, that scales critically follows the functional form

$$\chi \propto L^{-\alpha/\mu} F\left[(p - p_c)L^{1/\mu}\right] \tag{14}$$

where L is the scale of the system, p is the occupation probability, p_c is the critical probability, μ is the correlation exponent, and α is the critical exponent associated with the property χ. F is called a universal function that is specific to the process and is valid at all scales. Since the generated fractures are weakly correlated, the occupation probability (of any given cell) cannot be explicitly defined. However, this was overcome by considering the average probability that a given cell is occupied, i.e., the void area fraction. When studying flow rates, q, through fractures, Eq. 14 is rewritten as

$$q \propto L^{-t/\mu} F\left[(A_f - A_c)L^{1/\mu}\right] \tag{15}$$

where t is the transport exponent, and A_f and A_c are the void area fraction and critical void area fraction, respectively. The important aspect of Eq. 15 is that at threshold $(A_f - A_c = 0)$, the universal function reduces to a constant and the flow rate is dominated by the observation scale L raised to the exponent $-t/\mu$. Writing flow in this form allows the transport exponent and the universal function to be computed numerically.

A Monte Carlo simulation was performed using the fracture generation, fracture deformation and the flow models discussed earlier. First, a spanning probability analysis as a function of scale was performed on weakly correlated aperture distributions subjected to normal loading for the free and for the PBC. The spanning probability is the probability that a connected void path exists across the entire length of the fracture. This analysis illuminates the critical scaling regimes (if they exist) and critical threshold with respect to the deformation of the void spaces. Figure 5a and b shows the spanning probability for the five scales used in this study for both the free and the PBC. When a fracture is deformed under the free boundary conditions, no clear threshold in the flow is observed (Fig. 5a). The threshold appears to shift with scale. The free boundary conditions fail to produce a scaling system because one of the main assumptions in scaling theory is that, when dealing with a system of scale L, the moments of any subsample of scale, $L' = L/b$, are independent of the location from which the subsamples were taken. Yet in the case of the free boundary conditions, subsections taken from near the edges of the sample have higher contact areas than those taken from the center. Therefore, the threshold for free boundary conditions is dominated by edge effects.

However, when the PBC are used, a scaling behavior is observed with a clear scale-invariant fixed point. Using renormalization theory, the critical threshold at infinite scale was determined to be $A_c = 0.56$. Based on this

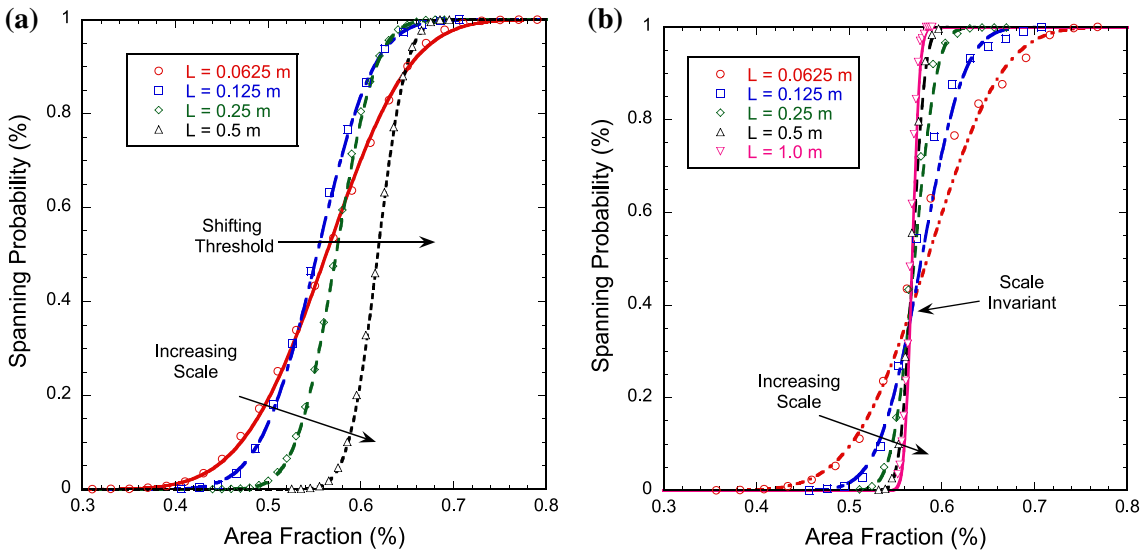

Fig. 5 Spanning probability as a function void area fraction showing the finite-size scaling of percolation threshold when **a** free boundary conditions and **b** PBC are used

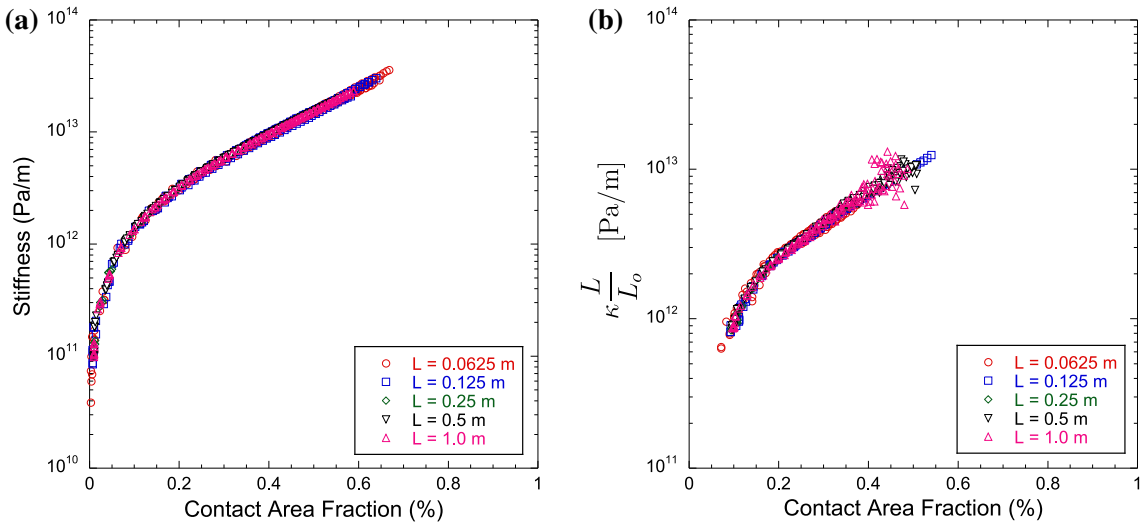

Fig. 6 Scaled fracture-specific stiffness as a function of contact area for a range of fracture sizes is shown when the computation is performed using **a** free boundary conditions and **b** PBC. Fracture-specific stiffness is scaled by the ratio of L/L_0

analysis, only the fractures deformed using the periodic boundary condition are used in the study of the scaling of the fluid flow–fracture-specific stiffness relationship.

5.2 Fracture-Specific Stiffness

At each scale, an initial unstressed aperture distribution was deformed numerically under a normal load. The average displacement vs. stress curve was generated based on 100 fracture patterns and was used to extract fracture-specific stiffness. Figure 6 shows the fracture-specific stiffness scaled by L/L_0 (subsection observation scale divided by the original scale of the fracture) as a function of contact area for the five scales used in this study. When either the free boundary conditions (Fig. 6a) or the PBC (Fig. 6b) are used, there is no critical scaling, but the calculated fracture stiffnesses for all scales lie on a single curve. Conceptually, this is much simpler than in the case of fluid flow. For fluid flow, the critical threshold occurs when a fracture no longer supports flow. The analogous property for fracture stiffness is the force that is transmitted through the fracture (normal to the fracture plane). The threshold is immediately realized when there is no contact between the two rough surfaces. Under this condition, no force can be transmitted through the fracture, thereby setting the fracture-specific stiffness to zero. As soon as points come into contact, the fracture resists deformation, leading to a nonzero stiffness. While the assumed boundary conditions had a profound effect on the spanning probability behavior, it was not as critical for calculating fracture-specific stiffness. As for the spanning probability, the scaled fracture-specific stiffness is plotted as a function of the contact area fraction in Fig. 6. It is observed that there is no critical scaling for both boundary conditions, only simple scaling by the ratio of the observation scales. The fractures in this study contain only short-range correlations, and the dependence of stiffness on length of the fracture is a simple proportional relationship. In the work of Morris (2012) and Morris et al. (2013), the fracture generation included longer-range correlations, and they found that the dependence of fracture-specific stiffness on scale differed from a simple proportionality.

5.3 Scaling of Hydromechanical Coupling

The previous sections described the thresholds for fracture-specific stiffness and the spanning probability. In this section, we present the scaling behavior of the coupled system, i.e., the flow–stiffness relationship. Only fractures simulated using PBC are considered because free boundary conditions do not generate fractures with a well-defined scaling threshold. For each scale, 100 fracture aperture distributions were stressed, numerically, to a load of 75 MPa in approximately 80 stress increments. For each increment in stress, the permeability was recomputed. The fluid flow finite-size scaling relationship (Eq. 15) is rewritten as

$$q \propto L^{-t/\mu} F\left[(A_{\mathrm{f}}(\sigma) - A_{\mathrm{c}}(\sigma))L^{1/\mu}\right] \tag{16}$$

where the only difference between Eqs. 15 and 16 is that in Eq. 16, the area fraction is a function of stress, σ. Flow values were chosen at threshold and plotted against their respective scales to extract the flow exponent. A power law fit to the data yielded the exponent $t/\mu = 2.4$. The scaled permeability is shown in Fig. 7. The permeability is scaled by a simple scaling (L/a^3 where a is the mean aperture for

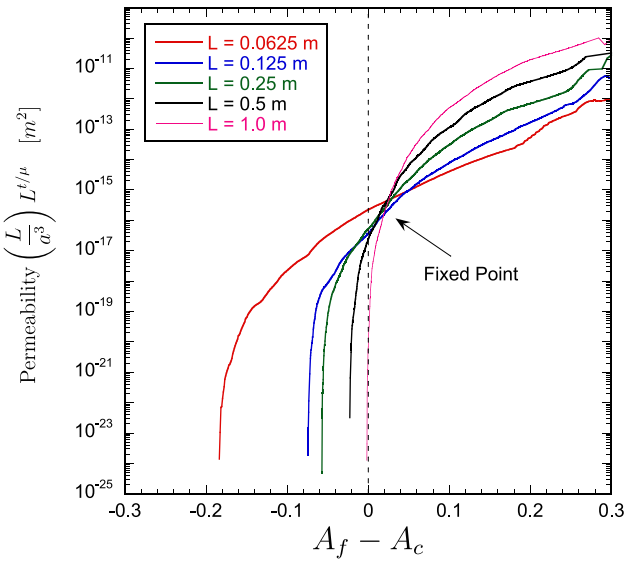

Fig. 7 Permeability shown as a function of area fraction. Permeability is scaled by the edge length, L, and the mean aperture, a, under zero load

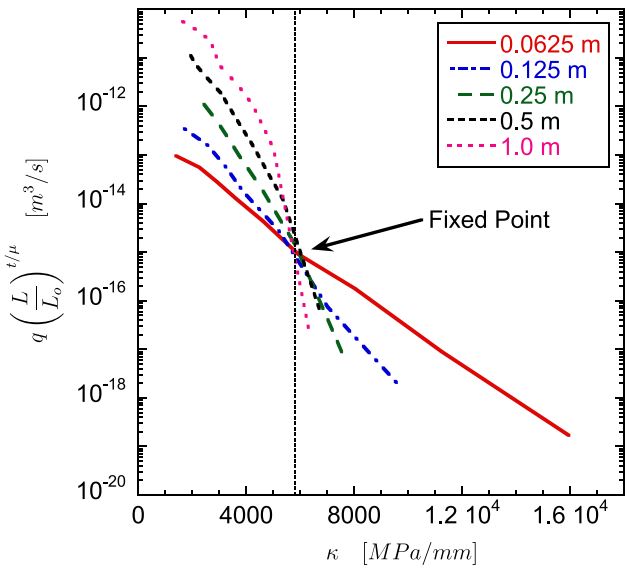

Fig. 8 Scaled permeability versus fracture-specific stiffness as a function of scale

the fracture at zero stress) and by critical scaling $L^{t/\mu}$. There is a fixed point above which flow increases with increasing size of the fracture and below which flow decreases with increasing fracture size.

In Fig. 8, scaled permeability is graphed as a function of fracture-specific stiffness. The flow–stiffness data are partially collapsed by scaling the flow rate by $(L/L_0)^{t/\mu}$, i.e., reflecting the prefactor of the universal scaling function in Eq. 16. Note that L has been replaced by the non-dimensional value L/L_0, where L_0 is the largest length used (1 m),

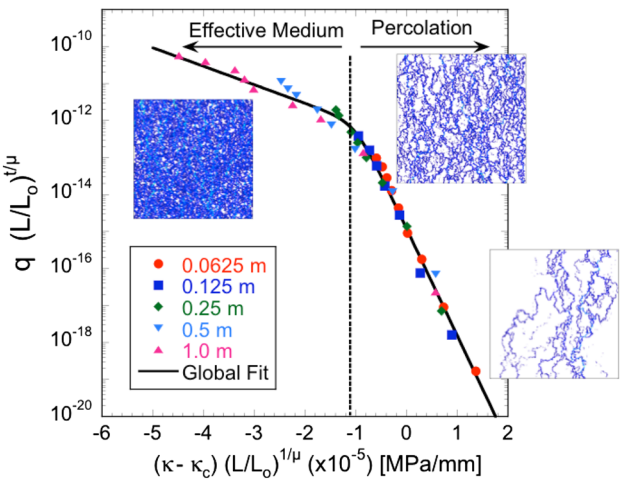

Fig. 9 Universal flow–stiffness function showing a full data collapse (after Petrovitch et al. 2013). The *solid line* is provided to guide the eye. The *insets* show the fluid velocity fields (in *blue*) in the effective medium regime, near threshold, and in the percolation regime (color figure online)

and q contains the same simple scaling (L/a^3) used in Fig. 7. This scaling also displays a fixed point near 5,800 MPa/mm, where each of the flow–stiffness curves cross at a single value, meaning that flow and stiffness are scale invariant at that point. The stiffness at this fixed point is defined as the critical stiffness, κ_c, and Eq. 16 can be rewritten as

$$q \propto L^{-t/\mu} F\left[(\kappa - \kappa_c) L^{1/\mu}\right] \tag{17}$$

where κ_c is the average stiffness at the critical threshold and is a key parameter in the final scaling relationship between flow and stiffness. From Fig. 8, it is apparent that fracture-specific stiffness is a surrogate for void area fraction as demonstrated by the observed fixed point and scaling behavior. Fracture-specific stiffness captures both the reduction in aperture and the reduction in void area as a fracture is loaded.

To complete the final data collapse, the stiffness was replotted as the difference $\kappa - \kappa_c$ and scaled by $(L/L_0)^{1/\mu}$, as shown in Fig. 9, while continuing to use $q(L/L_0)^{t/\mu}$ as the scaled fluid flow. With this scaling, the data at all scales fall on a single curve that has two clear regions with distinct slopes. The solid line in Fig. 9 is shown to guide the eye and represents the universal function of Eq. 17. There is a clear break in slope near $\kappa - \kappa_c \sim -1$, with each region above and below this value displaying an exponential dependence. The curve has a slope of -2 for $\kappa - \kappa_c > -1$ and a slope of –0.5 for $\kappa - \kappa_c < -1$. This break in slope divides the effective medium regime from the critical regime.

In the effective media regime ($\kappa - \kappa_c < -1$), multiple flow paths exist that support fluid flow through the fracture and are distributed nearly homogeneously across the

fracture plane (Fig. 9 inset in left) providing an almost sheet-like topology. As the normal stress increases into the critical regime ($\kappa - \kappa_c > -1$), the fluid velocity field is dominated by critical necks along the flow paths (Fig. 9 inset in right) and the flow paths take on a more string-like topology. The change in flow regimes is intimately related to the flow path topology and how it deforms under stress.

6 Conclusions

The key link between the hydraulic and mechanical properties of fractures is the fracture geometry and specifically how the geometry deforms under load. From this numerical study, a universal function was determined to exist that connects the hydraulic properties of a weakly correlated fracture to the fracture-specific stiffness, which is a property that can be probed using remote seismic techniques. The system under consideration contained both hydraulic and mechanical properties and therefore the potential for two non-trivial scaling behaviors. However, it was found that while the flow properties entered a critical scaling regime near the percolation transition, the mechanical properties of the fracture were found to have a simple scaling relationship with respect to void area fraction. Because of this, a global mechanical scaling exponent was not required to complete the full data collapse, leaving the entire system dependent on the transport exponent. This finding enabled fracture-specific stiffness to be used as a surrogate for void area fraction. The normal load becomes a key control variable in this relationship. When the load changes, contact areas are created that alter the cluster statistics of the fracture. Rather than the geometry of a fracture completely determining hydraulic properties, the deformation of the fracture topology under load is paramount. Thus, fracture-specific stiffness can replace the contact areas because the stiffness reflects the current state of the topology under a given load condition.

The discovery of the two regions in the universal scaling function is an important result from this study. At low stresses, the flow field across the fracture was homogeneous, almost sheet-like, and implies that flow covers most of the void spaces of the fracture. If smaller samples of the fracture are taken, the fluid velocity profiles of each subsection would be similar. However, as stress increases, flow paths begin to close, leaving only the main backbone of the original paths. At high stresses, many regions of the void space are without flow, leaving only narrow channels that support flow. If subsections of the fracture are studied, there would be many regions that had no fluid flow, giving the impression of a string-like topology. In this light, the change in slope of the flow–stiffness relationship can be understood as a transition from sheet-like to string-like topology.

From this analysis, it may be concluded that the geometry of a fracture and how it deforms provide all the necessary information to define a scaling relationship between the fracture-specific stiffness and fluid flow for fractures with weakly correlated aperture distributions. This scaling function is a stepping stone to a non-intrusive method to probe the hydraulic properties of single rock fractures in the subsurface. This has the potential to determine the future success of subsurface projects through characterization and monitoring techniques that can determine relative potential for fractures to support fluid flow. Future work requires an extension of this study to understand whether the scaling function holds for strongly correlated aperture distributions as well as for networks of fractures.

Acknowledgments This work is supported by the Geosciences Research Program, Office of Basic Energy Sciences US Department of Energy (DEFG02-97ER14785, DE-FG02-09ER16022), by the Geo Mathematical Imaging Group at Purdue University, the Purdue Research Foundation, and from the Computer Research Institute at Purdue University.

References

Bandis SC, Lumsden AC, Barton NR (1983) Fundamentals of rock joint deformation. Int J Rock Mech Min Sci 20(6):249–268

Barton NR, Bandis S, Bakhtar K (1985) Strength, deformation and conductivity coupling of rock joints. Int J Rock Mech Min Sci 22(3):121–140

Borodich FM, Onishchenko DA (1999) Similarity and fractality in the modelling of roughness by a multilevel profile with hierarchical structure. Int J Solids Struct 36(17):2585–2612

Brown SR (1989) Transport of fluids and electrical current through a single fracture. J Geophys Res 94(B7):9429–9438

Brown S, Scholz C (1985) Closure of random elastic surfaces in contact. J Geophys Res Solid Earth Planets 90(NB7):5531–5545

Brown SR, Stockman HW, Reeves SJ (1995) Applicability of the Reynolds equation for modeling fluid flow between rough surfaces. Geophys Res Lett 22(18):2537–2540

Cheng JT, Morris JP, Tran J, Lumsbaine A, Giordano NJ, Nolte DD, Pyrak-Nolte LJ (2004) Single-phase flow in a rock fracture: micro-model experiments and network flow simulation. Int J Rock Mech Min Sci 41:687–693

Cook NGW (1992) Natural joints in rock: mechanical, hydraulic, and seismic behavior and properties under normal stress. Int J Rock Mech Min Sci 29:198–223

Engelder T, Scholz CH (1981) Fluid flow along very smooth joints at effective pressure up to 200 megapascals. In: Mechanical behavior of crustal rocks, monograph 24, American Geophysical Union, pp 147–152

Gale JE (1987) Comparison of coupled fracture deformation and fluid models with direct measurements of fracture pore structure and stress-flow properties. In: 28th US Symposium on Rock Mechanics. A.A. Balkema, Tucson

Gale JE (1982) The effects of fracture type (induced versus natural) on stress-fracture closure-fracture permeability relationships. In: 23rd Symposium on Rock Mechanics. A.A. Balkema, Tucson

Glover PWJ, Matsuki K, Hikima R, Hayashi K (1998) Synthetic rough fractures in rocks. J Geophys Res Solid Earth 103(B5): 9609–9620

Greenwood JA, Williamson JBP (1966) Contact of nominally flat surfaces. In: Proceedings of the Royal Society of London. Series A, Mathematical and physical sciences, vol 295(1442), pp 300–319

Hopkins DL (1990) The effect of surface roughness on joint stiffness, aperture, and acoustic wave propagation. University of California, Berkeley

Hopkins DL (2000) The implications of joint deformation in analyzing the properties and behavior of fractured rock masses, underground excavations and faults. Int J Rock Mech Min Sci 37:175–202

Hopkins DL, Cook NGW, Myer LR (1990) Normal joint stiffness as a function of spatial geometry and surface roughness. In: International Symposium on Rock Joints. Loen, Norway

Jaeger JC, Cook NGW, Zimmerman R (2007) Fundamentals of rock mechanics, 4th edn. Wiley-Blackwell, New York

Kendall K, Tabor D (1971) An ultrasonic study of the area of contact between stationary and sliding surfaces. Proc R Soc Lond Ser A 323:321–340

Lambert CG (1994) Multipole-based algorithms for efficient calculation of forces and potentials in macroscopic periodic assemblies of particles. Duke University

Lomize GM (1951) Water flow through jointed rock (in Russian). Gosenergoizdat, Moscow

Morris JP (2012) A numerical investigation of the scaling of fracture stiffness. In 46th US Rock Mechanics/Geomechanics Symposium 2012. Curran Associates, Inc., Chicago, Illinois

Morris JP, Jocker J, Prioul R (2013) Exploring alternative characterizations of fracture stiffness and their respective scaling behaviors. In: 47th US Rock Mechanics/Geomechanics Symposium 2013. Curran Associates, Inc., San Francisco, California

Neuzil CE, Tracy JV (1981) Flow through fractures. Water Resour Res 17(1):191–199

Ng EG, Peyton BW (1993) Block sparse Cholesky algorithms on advanced uniprocessor computers. SIAM J Sci Comput 14(5):1034–1056

Nolte DD, Pyrak-Nolte LJ (1991) Stratified continuum percolation—scaling geometry of hierarchical cascades. Phys Rev A 44(10):6320–6333

Nolte DD, Pyrak-Nolte LJ (1997) Coexisting two-phase flow in correlated two-dimensional percolation. Phys Rev E 56(5): 5009–5012

Nolte DD, Pyrak-Nolte LJ, Cook NGW (1989) The fractal geometry of flow paths in natural fractures in rock and the approach to percolation. Pure Appl Geophys 131(1–2):111–138

Peitgen H, Saupe D (1988) The science of fractal images. Springer, New York

Petrovitch CL (2013) Universal scaling of flow-stiffness relationship in weakly correlated fractures. In: Physics 2013. Purdue University, West Lafayette, p 130

Petrovitch CL, Nolte DD, Pyrak-Nolte LJ (2013) Scaling of fluid flow versus fracture stiffness. Geophys Res Lett 40:2076–2080

Pyrak-Nolte LJ (1996) The seismic response of fractures and the interrelations among fracture properties. Int J Rock Mech Min Sci 33(8):787

Pyrak-Nolte LJ, Myer LR, Cook NGW, Witherspoon PA (1987) Hydraulic and mechanical properties of natural fractures in low permeability rock. In: Sixth International Congress on Rock Mechanics. A.A. Balkema, Montreal, Canada

Pyrak-Nolte LJ, Morris JP (2000) Single fractures under normal stress: the relation between fracture specific stiffness and fluid flow. Int J Rock Mech Min Sci 37(1–2):245–262

Pyrak-Nolte LJ, Cook NGW, Nolte DD (1988) Fluid percolation through single fractures. Geophys Res Lett 15(11):1247–1250

Pyrak-Nolte LJ, Myer LR, Nolte DD (1992) Fractures—finite-size-scaling and multifractals. Pure Appl Geophys 138(4):679–706

Raven KG, Gale JE (1985) Water flow in a natural rock fracture as a function of stress and sample size. Int J Rock Mech Min Sci 22(4):251–261

Renshaw CE (1995) On the relationship between mechanical and hydraulic apertures in rough-walled fractures. 24,636 100: 24,629–24,636

Schmidt KE, Lee MA (1991) Implementing the fast multipole method in three dimensions. J Stat Phys 63(5):1223–1235

Swan G (1983) Determination of stiffness and other joint properties from roughness measurements. Rock Mech Rock Eng 16:19–38

Timoshenko SP, Goodier JN (1970) Theory of elasticity. McGraw-Hill, New York

Tran JJ (1998) Efficient simulation of multiphase flow in three-dimensional fracture networks. Department of Computer Science and Engineering, Notre Dame University (Masters Thesis)

Tsang YW (1984) The effect of tortuosity on fluid flow through a single fracture. Water Resour Res 20(9):1209–1215

Tsang YW, Tsang CF (1987) Channel model of flow through fractured media. Water Resour Res 23:467

Walsh JB (1981) Effect of pore pressure and confining pressure on fracture permeability. Int J Rock Mech Min Sci 18(5):429–435

Walsh JB (1965) Effect of cracks on compressibility of rock. J Geophys Res 70(2):381

Watanabe N, Hirano N, Tsuchiya N (2008) Determination of aperture structure and fluid flow in a rock fracture by high-resolution numerical modeling on the basis of a flow-through experiment under confining pressure. Water Resour Res 44(6). doi:10.1029/2006WR005411

Witherspoon PA, Wang JS, Iwai K, Gale JE (1980) Validity of cubic law for fluid flow in a deformable rock fracture. Water Resour Res 16(6):1016–1024

Yang G, Myer LR, Brown SR, Cook NGW (1995) Microscopic analysis of macroscopic transport-properties of single natural fractures using graph-theory algorithms. Geophys Res Lett 22(11):1429–1432

Yang G, Cook NGW, Myer LR (1989) Network modelling of flow in natural fractures as a guide for efficient utilization of natural resources. In: Proceedings of 30th US Symposium on Rock Mechanics, pp 57–64

Yoshioka N, Scholz CH (1989) Elastic properties of contacting surfaces under normal and shear loads 2. Comparison of theory with experiment. J Geophys Res 94:1769–1770

Zimmerman RW, Bodvarsson GS (1996) Hydraulic conductivity of rock fractures. Transp Porous Media 23(1):1–30

Zimmerman RW, Chen DW, Long JSC, Cook NGW (1990) Hydro-mechanical coupling between stress, stiffness, and hydraulic conductivity of rock joints and fractures. In: Proceedings of the international symposium on rock joints. Balkema, Leon, Norway